RSC Advances

PAPER

View Article Online
View Journal | View Issue

Cite this: *RSC Adv.*, 2024, **14**, 5959

Adsorption of lead ions from wastewater using electrospun zeolite/MWCNT nanofibers: kinetics, thermodynamics and modeling study†

Urwa Mahmood, [a] Ali S. Alkorbi, [bc] Tanveer Hussain, [a] Ahsan Nazir, *[ad] Muhammad Bilal Qadir, *[ae] Zubair Khaliq, [fe] Sajid Faheem [a] and Mohammed Jalalah [bgh]

Heavy metal contamination in water is a serious environmental issue due to the toxicity of metals like lead. This study developed zeolite and multi-walled carbon nanotube (MWCNT) incorporated polyacrylonitrile (PAN) nanofibers *via* needleless electrospinning and examined their potential for lead ion adsorption from aqueous solutions. The adsorption process was optimized using response surface methodology (RSM) and artificial neural network (ANN) modeling approaches. The adsorbent displayed efficient lead removal of 84.75% under optimum conditions (adsorbent dose (2.21 g), adsorption time (207 min), temperature (48 °C), and initial concentration (62 ppm)). Kinetic studies revealed that the adsorption followed pseudo-first-order kinetics governed by interparticle diffusion. Isotherm analysis indicated Langmuir monolayer adsorption with improved 5.90 mg g^{-1} capacity compared to pristine PAN nanofibers. Thermodynamic parameters suggested the adsorption was spontaneous and endothermic. This work demonstrates the promise of electrospun zeolite/MWCNT nanofibers as adsorbents for removing lead from wastewater.

Received 11th November 2023
Accepted 31st January 2024

DOI: 10.1039/d3ra07720a

rsc.li/rsc-advances

1 Introduction

Over the past few decades, the uncontrolled discharge of industrial wastewater due to various chemical processes in industries such as PVC production, metal plating, pharmaceutical drug synthesis and dyes, pigment and pesticide manufacturing, *etc.*, has adversely contaminated water resources.[1] Wastewater enriched in heavy metals is a serious concern because of its ill health effects, such as neurological, cardiological, and kidney damage, cancer, and cognitive impairments.[2] Therefore, these heavy metals, *i.e.*, mercury (Hg^{+}), arsenic (As^{3+} & As^{5+}), chromium (Cr^{6+}), lead (Pb^{2+}), nickel (Ni^{2+}), *etc.*, seriously threaten the ecosystem.[3–5] Among all the heavy metals, lead is considered the most hazardous pollutant in wastewater, which, when ingested by humans, causes severe health issues such as cardiovascular disease, hemolytic anemia, Fanconi's syndrome, encephalopathy, nervous system disruption, hypertension, kidneys, and brain disorders.[6] The detrimental effects of heavy metals on numerous life forms have raised significant concerns among scientists and engineers, emphasizing the crucial need for their effective removal.[7,8]

Various water treatment techniques have been employed by researchers to reduce Pb^{2+}, including ion exchange,[9] flocculation,[10] membrane separation,[11] and adsorption.[12,13] Out of various proposed techniques, adsorption has been deemed a superior technology because it facilitates the swift removal of contaminants through a straightforward and cost-effective design. Furthermore, this process yields no harmful by-products, enhancing its overall environmental and practical appeal.[14] Various adsorbents have been proposed to remove Pb^{2+} from the polluted wastewater.[15]

Researchers have also evaluated the adsorption potential of fly ash (FA), an inexpensive and readily available industrial waste material, though it has a lower surface area when compared to other adsorbents.[16] To adsorb Pb^{2+} ions, researchers have produced FA using a "circulating fluidized bed combustion" method. The adsorption capacity of FA was found

[a]*Department of Textile Engineering, National Textile University, Faisalabad 37610, Pakistan. E-mail: urwa93@hotmail.com; hussain.tanveer@gmail.com; msajidfaheem@gmail.com*

[b]*Science and Engineering Research Center, Najran University, Najran 11001, Saudi Arabia*

[c]*Department of Chemistry, Faculty of Science and Arts at Sharurah, Najran University, Sharurah 68342, Saudi Arabia. E-mail: assalem@nu.edu.sa*

[d]*Laboratoire de Physique et Mécanique Textiles (LPMT), Université de Haute-Alsace | UHA, Mulhouse, France. E-mail: ahsan@ntu.edu.pk*

[e]*Department of Organic and Nano Engineering, Hanyang University, Seoul 04763, South Korea. E-mail: zubntu@yahoo.com; bilal_ntu81@hotmail.com*

[f]*Department of Materials, National Textile University, Faisalabad, 37610, Pakistan*

[g]*Department of Electrical Engineering, College of Engineering, Najran University, Najran 11001, Saudi Arabia. E-mail: msjalalah@nu.edu.sa*

[h]*Advanced Materials and Nano-Research Centre (AMNRC), Najran University, Najran 11001, Saudi Arabia*

† Electronic supplementary information (ESI) available. See DOI: https://doi.org/10.1039/d3ra07720a

to be up to 51 mg g^{-1} with a dosage of 5 g L^{-1} and followed the pseudo-II order and Freundlich isotherm kinetics.[16,17] Abdullah *et al.* incorporated manganese oxide in electrospun PAN nanofibers (ACNF/MnO_2) and reported that the Pb^{2+} percentage removal was higher in the case of ACNF and ACNF/MnO_2 as compared to granules of activated carbon.[18] Mikal *et al.* prepared zinc oxide nanoparticles (ZnO) decorated with PAN nanofibers using electrospinning for the Pb^{2+} adsorption. The adsorption was found to be exothermic and followed a pseudo-second order kinetic model.[19]

The current study incorporated ethylenediaminetetraacetic acid-activated MWCNTs and zeolite into electrospun nanofibers. These nano-adsorbents were examined for their ability to adsorb Pb^{2+} ions from an aqueous solution, with factors such as adsorbent dose, temperature, initial concentration, and contact time being considered. Pb^{2+} ions' adsorption onto nano-adsorbents was predicted using response surface methodology and artificial neural network approaches, which were not previously reported for these nano-adsorbents. The data collected from the adsorption studies were analyzed for kinetics, isotherms, thermodynamics, and equilibrium studies.

2 Materials and methods

Multiwalled carbon nanotubes (MWCNTs) with a length of 10–30 μm and diameter of 10–20 nm were procured from SAT Nano Technology Material Co., Ltd, China. Polyacrylonitrile (PAN, analytical grade), with a molecular weight (M_w) of 150 000 g mol^{-1}, was obtained from Exlan Corp, Japan. Coal fly ash was obtained from Sitara Chemicals, Pakistan, whereas ethylenediaminetetraacetic acid (EDTA), nitric acid (HNO_3), sulphuric acid (H_2SO_4), phosphoric acid (H_3PO_4), dimethylformamide (DMF), and lead nitrate ($Pb(NO_3)_2$) salt of lab grade with 99.9% purity were supplied by Sigma-Aldrich, Germany.

2.1. Activation of MWCNTs

For the activation of MWCNTs, 0.1 g of MWCNTs were dispersed ultrasonically in 50 ml of ethanol for 2.5 h to obtain a homogeneous dispersion. Then, 1.5 mmol of EDTA was added to 30 ml of ethanol, followed by the gradual addition of MWCNTs/ethanol into the solution. The solution was continuously stirred at 65–70 °C for 12 h. MWCNTs were then vacuum filtered and washed ten times. The activated MWCNTs (ACNTs) were dried at 60 °C in an oven (Thermo Fisher Scientific, United States).

2.2. Synthesis of zeolite

Coal fly ash was subjected to drying in an oven at 80 °C overnight to remove any retained moisture. The characterization of raw coal fly ash and zeolite is mentioned in the ESI file.† A mixture containing 16 M of HNO_3, 18 M of H_2SO_4, and 18 M of H_3PO_4, with a volume ratio of 40 : 20 : 40, respectively, was prepared in a sealed glass bottle. 5 g of coal fly ash was added to the acid mixture and placed on the magnetic stirrer for 3–4 h at 125 °C. The zeolite was filtered and rinsed several times with distilled water. The obtained zeolite was then dried at 110 °C for 6 h.[20]

2.3. Fabrication of nanofibrous membrane

PAN 8% (w/v) was dissolved in DMF while stirring for 12 h to get a homogenous dope solution. A weighed amount of activated MWCNTs was dispersed in the PAN solution and sonicated for 6 h to obtain a homogenous dispersion. The zeolite was added to the solution, followed by sonication for another 6 h before electrospinning.

The prepared dope dispersion was poured into a liquid carriage and placed in a needleless electrospinning machine (Nanospider, ELMARCO, Czech Republic). The operating parameters for the electrospinning were set at a voltage of 40 kV,

Fig. 1 Electrospinning process for the development of adsorbent.

Table 1 Details of pre-trials

Sample ID	PAN concentration	Concentration of activated MWCNTs	Concentration of zeolite
A1	8%	100 mg	50 mg
A2	8%	100 mg	100 mg
A3	8%	100 mg	150 mg
A4	8%	100 mg	200 mg

a carriage speed of 90 mm s^{-1}, and an electrospinning distance of 200 mm. The process has been presented in Fig. 1.[21]

The following pre-trials were performed as mentioned in Table 1 and then subjected to characterizations.

The sample containing maximum zeolite concentration was selected based on SEM results (as mentioned in Section 3.1 & Fig. 2) for further batch adsorption studies.

2.4. Statistical modeling

The adsorptive behavior of Pb^{2+} on the nano-adsorbent was studied and optimized using statistical techniques, *i.e.*, Response Surface Methodology (RSM). The adsorbent dose, adsorption time, and temperature were selected as independent factors to study their influence on the Pb^{2+} removal efficiency. The central composite design of the experiment (CCD) was developed using Design Expert Pro. The selected experimental factors and their respective levels are given in Table 2.

Table 2 Factors and their levels of CCD

Factors	Symbols	Levels	
		Low	High
Adsorbent dose (g)	x_D	0.25	2.5
Adsorption time (min)	x_t	10	300
Temperature (°C)	x_T	20	50
Initial concentration (mg l^{-1})	x_{IC}	50	400

The batch adsorption experimentation was implemented according to the design matrix, containing 30 runs, as mentioned in Table 3.

2.5. Artificial neural network modelling

Artificial Neural Network (ANN) is a mathematical modelling tool, inspired by the functioning of human-brain.[22] ANN is based on the principles of the Takagi–Sugeno fuzzy inference system using input and output layers with one or multiple

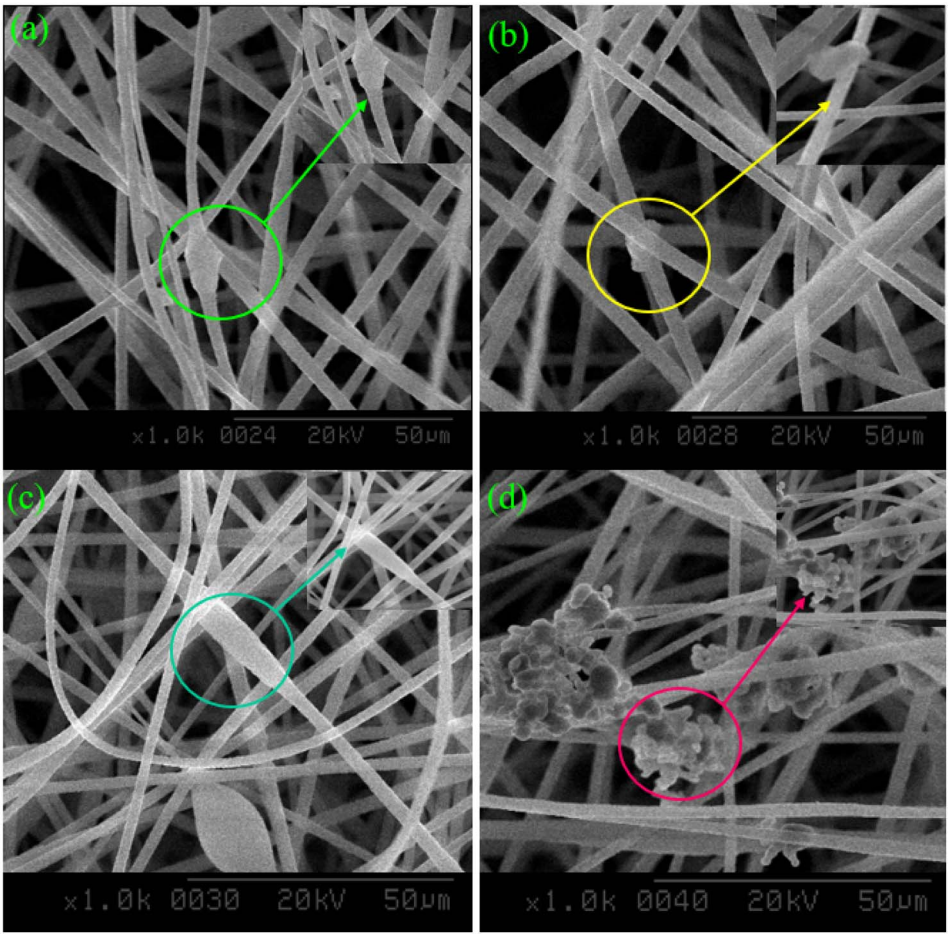

Fig. 2 SEM micrographs of developed (a) A1, (b) A2, (c) A3, and (d) A4 adsorbents.

Table 3 Design matrix for the adsorption experimentation

Sr.	Dose (g)	Time (min)	Temperature (°C)	Initial concentration (mg l^{-1})
1	1.375	155	35	225
2	1.375	155	35	225
3	2.5	155	35	225
4	0.25	10	50	50
5	0.25	155	35	225
6	2.5	10	20	50
7	2.5	300	20	400
8	0.25	300	20	50
9	2.5	10	50	400
10	1.375	155	35	225
11	1.375	155	35	225
12	2.5	10	50	50
13	0.25	10	20	50
14	1.375	10	35	225
15	0.25	10	50	400
16	0.25	300	50	50
17	1.375	300	35	225
18	1.375	155	50	225
19	0.25	300	20	400
20	1.375	155	35	400
21	1.375	155	20	225
22	0.25	10	20	400
23	2.5	300	50	400
24	2.5	300	50	50
25	1.375	155	35	225
26	1.375	155	35	225
27	2.5	10	20	400
28	0.25	300	50	400
29	1.375	155	35	50
30	2.5	300	20	50

hidden layers (neurons).[23] These neurons predict the interrelation of input and output layers.[24]

2.6. Characterization

2.6.1. Scanning electron microscopy (SEM). The surface textural and topological features were analyzed on Nova SEM (FEI nano-SEM 450, Czech Republic) at 10 kV accelerating voltage using a secondary electron detector. The prepared electrospun adsorbents were attached to the metallic stubs using double-sided conductive tape. The gold sputtering was applied on the adsorbents in the N_2 environment using a Sputter coater (Desk V, Denton Vacuum, USA) for 15 s.

2.6.2. Energy dispersive X-ray spectroscopy (EDX). The elemental composition of electrospun adsorbents was determined using EDX (INCA X'Act, Oxford Instruments, England).

2.6.3. Fourier transform infrared spectroscopy (FTIR). Electrospun adsorbents were desiccated and mixed with KBr powder to form a pallet using a hydraulic press. The prepared pellet was analyzed using FTIR Spectrometer (ZnSe-HATR, 24 Module, Perkin Elmer-Spectrum two, United States) under an average wavenumber ranging from 4000 to 500 cm^{-1} using 20 scans, and to identify surface functional groups.

2.6.4. Point of zero charge (PZC). To determine the point of zero charge (PZC) of the developed adsorbents, solutions with pH ranging from 2 to 13 were prepared using 0.1 M sodium hydroxide (NaOH) and 0.1 M acetic acid (CH_3COOH). Each solution's initial pH (pH_0) was measured using a pH meter (AD1000, Adwa, Hungary). 0.15 g adsorbents were added to the Erlenmeyer flask containing each solution and shaken for 24 h using an orbital shaker (SHO-2D, WISD, USA). The final pH of the solutions after 24 h was then measured, and the pH gradient was then calculated using eqn (1) below:

$$\Delta pH = pH_f - pH_0 \quad (1)$$

where, ΔpH is the pH gradient, pH_0 is the initial pH of solution and pH_f is the final pH of solution measured after 24 h.

2.7. Batch adsorption studies

Adsorption capacities of optimized absorbents towards Pb^{2+} ions were investigated in batch experimentation. Each batch adsorption experiment was performed according to the developed design of experiment. After each experiment, the adsorbate was filtered using a sterile CA membrane filter having a pore size of 0.22 μm. The filtered adsorbate was diluted with double distilled water and further analyzed using the "Inductively Coupled Plasma Optical Emission Spectrometer" (ICP-OES 5110, Agilent, USA) at 220.353 nm wavelength. The 100 ppm stock solution was prepared using $Pb(NO_3)_2$ and 1% HNO_3, which was then diluted to prepare calibration solutions of 0.2 ppm, 0.3 ppm, 0.5 ppm, 1 ppm, 1.5 ppm, and 2 ppm. The uptake capacity of Pb^{2+} adsorption at equilibrium and adsorption efficiency was calculated using eqn (2) and (3):[25,26]

$$q_e = \frac{(c_i - c_e)}{m} \times V \quad (2)$$

$$\text{Removal efficiency } (\%) = \frac{(c_i - c_e)}{c_i} \times 100 \quad (3)$$

where q_e (mg g^{-1}) is the uptake capacity at equilibrium, c_i (mg l^{-1}) and c_e (mg l^{-1}) are the initial and equilibrium concentrations, respectively, m (g) is the dry mass of the adsorbent, and V (l) is the solution volume.

The effect of time and kinetic studies were performed by varying adsorption time *i.e.*, 10 to 300 minutes while keeping other parameters constant. Weighed amount of adsorbent was added to 100 ppm Pb^{2+} solution, followed by orbital shaking and adsorbate was filtered and diluted prior to ICP analysis. Different temperatures (293 K to 323 K) were employed to study the effect of temperature and thermodynamics while keeping other parameters constant. Adsorption experiments were conducted at different temperatures and then subjected to ICP analysis.

2.7.1. Adsorption kinetics. The investigation of adsorption kinetics plays a crucial role in analyzing the adsorption process, as it provides valuable experimental parameters for designing aqueous solution systems.[27] The adsorption kinetic study of the adsorbent was performed using the following non-linear models: pseudo-first order, pseudo-second order, and pseudo-*n*th order. Intra-particle diffusion (Weber and Morris) model and Bangham's model define the diffusion mechanism during adsorption.

The pseudo-first order model assumes the Pb^{2+} adsorption is a relationship between the rate of occupied adsorption sites by the Pb^{2+} ions and the unoccupied sites available on the surface of adsorbents. It indicates the adsorption rate is directly proportionate to the available adsorption sites on the adsorbent's surface. A non-linear equation for the pseudo-first order kinetic model is as follows.[28]

$$q_t = q_e(1 - \exp(-k_0 t)) \quad (4)$$

q_e (mg g^{-1}) and q_t (mg g^{-1}) are the concentration of Pb^{2+} adsorbed at equilibrium and at a specific time (t) respectively, k_o (min^{-1}) is the adsorption rate constant of the pseudo-first order model.

The pseudo-second order describes the chemisorption, which involves the creation of chemical bonds between adsorbent and adsorbate and is represented in mathematical form.[29,30]

$$q_t = \frac{{q_e}^2 k_1 t}{1 + k_1 q_e t} \quad (5)$$

where k_1 (g mg^{-1} min) is the constant related to the pseudo-second order model.

The pseudo-*n*th order model is non-linear and provides the accurate kinetic processes order depending on the adsorption capacity of the adsorbent. The expression of the pseudo-*n*th order model in the case of adsorption is given as.[31]

$$q_t = q_e - \left(q_e^{(1-n)} + (n-1)K_n t\right)^{\frac{1}{(1-n)}} \quad (6)$$

where, K_n ((mg $g^{-1})^{1-n}$ min^{-1}) is the constant for pseudo-*n*th order and n is the reaction order to concerning the corresponding concentration.

The adsorption data is further analyzed by the Weber and Morris kinetic model (intra-particle diffusion), which determines the diffusion mechanism of the Pb^{2+} adsorption. The equation of the Weber and Morris model is.[32]

$$q_t = k_{wb}(t^{1/2})\varnothing_1 \quad (7)$$

where, $\varnothing_1$ (mg g^{-1}) is the intercept presenting the thickness of the boundary layer and k_{wb} (mg g^{-1} $min^{-1/2}$) is the diffusion rate constant. The Weber and Morris model generates a graphical representation by plotting q_t *vs.* $t^{1/2}$.

Bangham's model evaluates that the Pb^{2+} ions adsorption is based on the pore diffusion mechanism and is expressed as.[33]

$$\log\left(\frac{c_i}{c_i - q_t W}\right) = \log\left(\frac{k_b}{2.303V}\right) + \delta \log t \quad (8)$$

where, q_t (mg g^{-1}) is the concentration of Pb^{2+} adsorbed at a specific time (t), k_b is the rate of adsorption constant of Bangham's model ($min^{-\delta}$) and δ is the constant, c_i is the initial concentration of Pb^{2+} in the solution (mg l^{-1}), V is the volume of adsorbate (l), and W is the mass of adsorbent (g).

2.7.2. Error Analysis. Error analysis is crucial to evaluate the optimum fit of kinetic models on the adsorption results. The coefficient of determination (R^2) estimates the model's validity for experimental results, and its higher value depicts the goodness of fit to data. However, the minimum error value and the highest coefficient of determination are considered the best fit for adsorption results.[34] The expression for error function, *i.e.*, Sum of Square of Errors (SSE) is mentioned as eqn (9).[35]

$$\mathrm{SSE} = \sum_{i=1}^{n} \left(Q_{e(cal.)} - Q_{e(actual)}\right)^2 \quad (9)$$

where $Q_{e(cal.)}$ and $Q_{e(actual)}$ are the calculated and actual concentrations of adsorbate at equilibrium, respectively and n is the number of data points.

2.7.3. Adsorption isotherms. Adsorption isotherms were employed to determine the interaction of an absorbent with adsorbate. Langmuir and Freundlich isotherm models are used to investigate the adsorption behavior of the adsorbent.[36] The adsorption isotherm study was performed by varying the initial concentration of Pb^{2+} from 10 to 150 ppm. Langmuir isotherm was employed, which assumes that the adsorbent surface has homogenous active sites and the adsorption is a monolayer adsorption. The Langmuir model in its non-linear form is expressed as follows;[37]

$$q_e = \frac{q_{max} K_l C_e}{1 + (K_l C_e)} \quad (10)$$

where, q_e (mg g^{-1}) is the uptake capacity at equilibrium, C_e (mg l^{-1}) is the concentration of ions at equilibrium, q_{max} (mg g^{-1}) is the maximum capacity of the adsorbent and K_l (l mg^{-1}) is the Langmuir constant related to the adsorption's free energy. The Freundlich model is considered an empirical approach that predicts the heterogeneous surface and adsorption that in multilayers of adsorbents. The equation of the Freundlich model is;[38]

$$q_e = K_F {C_e}^{1/n} \quad (11)$$

where, q_e (mg g^{-1}) is the uptake capacity at equilibrium, K_F (mg g^{-1} (l $mg)^{-1/n}$) is associated to the adsorption capacity of the developed adsorbent, and C_e (mg l^{-1}) is the Pb^{2+} ions concentration at equilibrium. The value of '*n*' should be between 1 and 10, as it presents the intensity of the adsorption process.

2.7.4. Thermodynamics of adsorption. The nature and favorability of the adsorption were determined using the thermodynamic analysis of adsorption. The pertinent thermodynamic parameters include Gibbs free energy (ΔG°), enthalpy (ΔH°), and entropy (ΔS°) calculated using the following equations:[39]

$$\Delta G^\circ = -RT \ln K_{th} \quad (12)$$

$$\Delta G^\circ = \Delta H^\circ - T\Delta S^\circ \quad (13)$$

$$\ln K_{th} = \frac{\Delta S^\circ}{R} - \frac{\Delta H^\circ}{RT} \quad (14)$$

where, T (K) is considered as the absolute temperature, K_{th} is the adsorption constant at equilibrium, R (kJ mol^{-1} K^{-1}) is the gas constant, ΔH° (kJ mol^{-1} K^{-1}) is the change in enthalpy in adsorption, ΔS° (kJ mol^{-1} K^{-1}) is the change in entropy in the adsorption process, ΔG° is the change in Gibbs free energy. The

ΔH° and ΔS° both are determined by the Van't Hoff plot of $1/T$ and $\ln K_{th}$.[40]

3 Results and discussion

3.1. SEM analysis

SEM micrographs ascertain the morphological structure of the developed adsorbents, as shown below in Fig. 2. The micrographs reveal that the nanofibers were loaded with the composite of ACNTs, and zeolite, as marked in Fig. 2. By incorporating the ACNTs and zeolite, the PAN nanofibers possess a more irregular and rougher surface. The roughness on the surface of nanofibers can also be due to the evaporation of DMF.[41] The SEM analysis indicated that the incorporation of ACNTs and zeolite well in nanofibers.

Moreover, the A4 adsorbent has a highly rough and irregular surface, which could be due to higher concentrations of ACNTs, and zeolite exposed to the surface, thus improving the surface area of nanofibers.[42] SEM analysis of the A4 adsorbent confirmed the presence of ACNTs and zeolite clusters on the nanofibers' surface and in the core. Incorporating highly conducting ACNTs into PAN results in the high charge density of the spinning dope solution and the excess of charge carriers present on the jet surface, leading to the formation of defect-free and finer fibers.[43,44]

EDX analysis confirmed the incorporation of zeolite and ACNTs into PAN nanofibers, and the elemental composition is mentioned in Table 4. It was evident that the adsorbents contained traces of aluminum, copper, silicon, and titanium due to the presence of zeolite and high weight % of carbon as the contribution of ACNTs embedded in the nanofibers. The presence of ACNTs and zeolite in the nanofibers led to the formation of more active sites and high surface area, contributing to the high removal efficiencies.[45,46]

Table 4 Elemental composition of A1, A2, A3, and A4 adsorbents

Adsorbents	Elements	Weight, %
A1	Carbon	84.59
	Oxygen	12.87
	Aluminum	0.29
	Silicone	0.51
	Copper	0.36
	Gold	1.25
	Titanium	0.13
A2	Carbon	86.68
	Oxygen	10.45
	Aluminum	0.39
	Silicone	0.62
	Copper	0.45
	Gold	1.23
	Titanium	0.18
A3	Carbon	87.37
	Oxygen	9.44
	Aluminum	0.55
	Silicone	0.74
	Copper	0.51
	Gold	1.18
	Titanium	0.21
A4	Carbon	89.77
	Oxygen	6.93
	Aluminum	0.67
	Silicone	0.84
	Copper	0.53
	Gold	1.01
	Titanium	0.25

3.2. FTIR analysis

Fig. 3 represents the IR spectrum of the developed electrospun composite adsorbents (A1, A2, A3, and A4). The overlapping absorption peaks in the qualitative FTIR analysis of composite adsorbents show that identical bands are present in the adsorbents which concludes that by changing the concentration of composites (zeolite/ACNTs) the IR spectra of all adsorbents does not show any significant change.[47] The use of H_2SO_4 in the synthesis of zeolite results in reducing the number of hydroxyl groups, due to a dehydrating nature of H_2SO_4. The peaks at 2915 and 2851 cm^{-1} may be ascribed to the sp^3 CH stretching of the hydrocarbon structure that confirmed the presence of aliphatic acid and OH vibrations, respectively.[20] The sharp peak at 2244 cm^{-1} appears due to the stretching of the nitrile group (C≡N), evidenced by the existence of PAN in adsorbents.[42,48]

The peak at 1739 cm^{-1} assigned to the C=O group of carboxyl and lactones, which indicates the presence of zeolite in the adsorbents. The zeolite exhibits oxygenated acid groups on its surface, such as carboxylic, hydroxyl, and lactone.[49] Whereas, at 1676 cm^{-1}, the peak indicates the C=C stretching of aromatic rings.[50,51] The peak at 1444 cm^{-1} is assigned to the O–H bending associated with the carboxylic group. An asymmetric stretching of the S=O group that appears at 1367 cm^{-1} may be associated with the functional sites exiting on the zeolite's surface.[52] The peak at 1036 cm^{-1} corresponds to the EDTA's vibrational stretching and bending caused by the N–H group which shows the EDTA activation.[53] The IR spectra verified the presence of functional sites that can serve as the potential adsorption sites in the Pb^{2+} ions adsorption and successful incorporation of zeolite/ACNTs in PAN nanofibers.

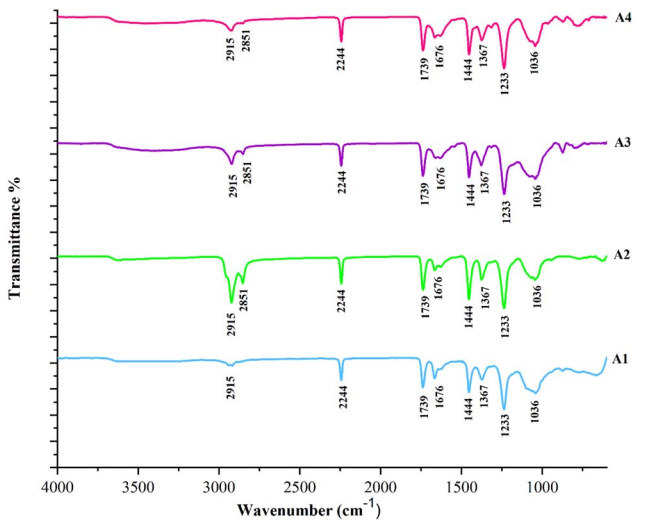

Fig. 3 FTIR spectra of developed adsorbents (A1, A2, A3, and A4).

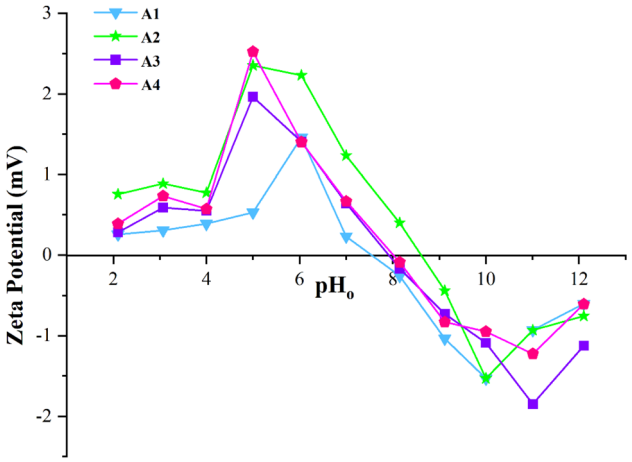

Fig. 4 Isoelectric point of A1, A2, A3, and A4 adsorbents.

3.3. Point of zero charge

Fig. 4 presents the effect of pH (2–12) on the surface charge of the developed adsorbents (A1, A2, A3 and A4). The isoelectric points are 7.5, 7.9, 8.0, and 8.6 for A1, A2, A3, and A4 adsorbents. These values indicate that the surface of adsorbents possesses a negative charge above their isoelectric point and positively charged below their isoelectric point. At the isoelectric point, the adsorbent's surface carries an equal number of positive and negative charges. Thus, at this point, the net charge on the surface is zero, which means it is electrically neutral.[54,55]

As the pH of Pb^{2+} contaminated aqueous solution is higher than the isoelectric point of adsorbents, the surface of adsorbents possesses negative charges. Thus, the negative surface of adsorbents is favorable for binding Pb^{2+} ions (cations).[56] However, the surface becomes positively charged when the Pb^{2+} contaminated aqueous solution's pH is lower than the adsorbent's isoelectric point. This phenomenon considerably limits the electrostatic interaction and ion exchange between adsorbent and adsorbate, thus stalling the cations (Pb^{2+}) adsorption.[57,58]

3.4. Statistical analysis

The Pb^{2+} adsorption studies were performed according to the DOE given in Table 2. The removal efficiency% of the experiments is mentioned in Table 5.

The quadratic model was selected in regression modeling to define the relationship between independent and dependent variables to predict the Pb^{2+} removal efficiency of the developed adsorbent. The mathematical regression equation for the response (removal efficiency %) prediction is as follows.

Table 5 Removal efficiency % of adsorbents according to DOE

Sr.	Dose (g)	Time (min)	Temperature (°C)	Initial concentration (mg l^{-1})	Removal efficiency (%)
1	1.375	155	35	225	68.35
2	1.375	155	35	225	70.58
3	2.5	155	35	225	76.47
4	0.25	10	50	50	30.13
5	0.25	155	35	225	32.96
6	2.5	10	20	50	38.41
7	2.5	300	20	400	51.32
8	0.25	300	20	50	34.48
9	2.5	10	50	400	33.73
10	1.375	155	35	225	67.09
11	1.375	155	35	225	70.16
12	2.5	10	50	50	45.92
13	0.25	10	20	50	18.47
14	1.375	10	35	225	29.74
15	0.25	10	50	400	19.35
16	0.25	300	50	50	39.97
17	1.375	300	35	225	72.36
18	1.375	155	50	225	75.92
19	0.25	300	20	400	20.16
20	1.375	155	35	400	53.69
21	1.375	155	20	225	57.26
22	0.25	10	20	400	12.98
23	2.5	300	50	400	72.81
24	2.5	300	50	50	89.75
25	1.375	155	35	225	67.79
26	1.375	155	35	225	69.93
27	2.5	10	20	400	30.96
28	0.25	300	50	400	25.31
29	1.375	155	35	50	81.81
30	2.5	300	20	50	66.94

$$Y_{Re} = 4.21 + 32.26x_D + 0.26x_t + 0.39x_T - 0.025x_{IC} + 0.036x_D x_t + 0.096x_D x_T - 0.002x_D x_{IC} + 0.0008x_t x_T - 6.31 \times 10^{-5} x_t x_{IC} - 0.00028x_T x_{IC} - 9.88{x_D}^2 - 0.00077{x_t}^2 - 0.003{x_T}^2 + 1.72 \times 10^{-5}{x_{IC}}^2 \quad (15)$$

where, Y_{Re} is the predicted response (removal efficiency), x_D, x_t, x_T, x_{IC} are the independent variables, *i.e.*, dose, time, temperature, and initial concentration, respectively. It can be observed from eqn (15) that the variables, *i.e.*, dose, time, and temperature, showed a significant effects on the adsorption capacity. However, the x_{IC} has a negative value, which means by increasing the initial concentration by optimum conditions, adsorption capacity will decrease. The positive value in the above-mentioned equation indicates that the variable favors the adsorption process while negative values represent inverse relationship between variables and adsorption efficiency.[59]

The effectiveness of developed model is quantified by the RSM model equation and ANOVA (analysis of variance) helps to determine the contribution of each variable towards explaining the variance in the response variable. Variables with low *p*-values in the ANOVA analysis are considered statistically significant and have a more substantial impact on the response.

3.4.1. Analysis of variance. The ANOVA analysis was performed using Minitab 18 Software, and the results are mentioned in Table 6.

As per the data mentioned above in Table 4, the regression model has a high degree fit and is verified by the coefficients of regression, *i.e.*, R^2 (0.9603), R^2 adj (0.9233), and R^2 predicted (0.7994). The value of $R^2 = 0.9603$ indicates that the model can predict the data and the experimental data is very close to the estimated data.[60] These values suggest that the mathematical model explains the relationship between the response (removal efficiency) and the process variables (dose, time, temperature, and initial concentration).[61] The significance of linear (x_D, x_t, x_T, x_{IC}), interactive ($x_D x_D$, $x_t x_t$, $x_T x_T$, $x_{IC} x_{IC}$) and quadratic parameters ($x_D x_t$, $x_D x_T$, $x_D x_{IC}$, $x_T x_{IC}$) on the response (removal efficiency) can be evaluated by the *p*-values and *F*-values.[62,63]

Table 6 Analysis of variance for Pb^{2+} removal using ACNTs–zeolite supported adsorbents

Source	DF	Adj SS	Adj MS	*F*-value	*p*-Value
Model	14	13 934.33	995.31	25.94	<0.0001
x_D	1	4125.41	4125.41	107.52	<0.0001
x_t	1	2530.90	2530.90	65.96	<0.0001
x_T	1	576.83	576.83	15.03	0.0015
x_{IC}	1	875.78	875.78	22.82	0.0002
$x_D x_t$	1	538.30	538.30	14.03	0.0019
$x_D x_T$	1	41.97	41.97	1.09	0.3122
$x_D x_{IC}$	1	3.00	3.00	0.078	0.7836
$x_t x_T$	1	44.34	44.34	1.16	0.2994
$x_t x_{IC}$	1	41.08	41.08	1.07	0.3172
$x_T x_{IC}$	1	8.58	8.58	0.22	0.6432
${x_D}^2$	1	405.41	405.41	10.57	0.0054
${x_t}^2$	1	677.90	677.90	17.67	0.0008
${x_T}^2$	1	1.04	1.04	0.027	0.8716
${x_{IC}}^2$	1	0.72	0.72	0.019	0.8932
Residual	15	575.55	38.37		
Lack of fit	10	565.42	56.54	27.90	0.03
Pure error	5	10.13	2.03		
Total	29	14 509.88			

The *F*-values for dose, time, temperature, and initial concentration are 107.52, 65.96, 15.03, and 22.82, respectively, showing that varying these parameters directly influences the removal efficiency, suggesting that the models are significant. At the same time, the *p*-values of model, independent variables (dose, time, temperature, and initial concentration), and lack of fit is less than the 0.05 which showed that these factors are significant and validate the adsorption process and also influence removal efficiency.

3.4.2. Residual plots. A scattering pattern of studentized residuals as shown in Fig. 5(a) lies around the diagonal axis, implying that the results follow a normal distribution with no deviation from the diagonal axis showing no skewness. If the data does not follow normal distribution, the probability of achieving accurate results decreases. No skewness in the data implies that the *p*-values associated with the *F*-test are accurate. The scattering pattern of residuals, Fig. 5(b), entails that no ignored factors exist that significantly affect removal efficiency (response). The plot of residuals implies a randomly scattered pattern followed by the student residuals, and the variation in residuals does not observe any specific trend, as shown in Fig. 5(b). This indicates that systematic errors are not inherited in observations. The close relationship between the actual and predicted values signifies that model adequacy allows for eliminating the insignificant factors. The relation between actual and predicted results is demonstrated in Fig. 5(c).

3.4.3. Surface plots. The 3D surface plots for the impact of dose, time, and temperature on the removal efficiency of Pb^{2+} ions are indicated in Fig. 5(d)–(f). Fig. 5(d)–(f) has curvy surfaces of plots showing a synergistic relationship between adsorbent dose, adsorption time, and temperature. The removal efficiency increases with the increase in the adsorbent dose. As a result of increasing the dose, the number of active sites for adsorption and the oxygenated functional groups increases.[64,65] The adsorbent dose has a substantial effect on the Pb^{2+} removal efficiency.

Similarly, the 3D plot Fig. 5(d) illustrates that increasing the adsorption time increases the removal efficiency, allowing enough time for adsorption until it reaches equilibrium.[66] Further, it can also be observed that the increasing temperature contributes to the removal efficiency.[67] However, Fig. 5(f) shows that adsorption decreases by increasing the initial concentration of Pb^{2+} ions. The surface plots depict that the removal efficiency directly relates to the dose, time, and temperature while indirectly related to the initial concentration of Pb^{2+} ions. These results are consistent with the regression equation of the model (eqn (15)).

3.4.4. Optimization of response. The optimization of different variables to get the best operational parameters to achieve outstanding efficiency for Pb^{2+} adsorption was performed by setting the condition for a response as "maximum." The response optimizer plot for the developed adsorbent is shown in Fig. 6. It can be evaluated from the plot that the predicted optimum parameters are adsorbent dose (2.21 g), adsorption time (207 min), temperature (48 °C), and initial

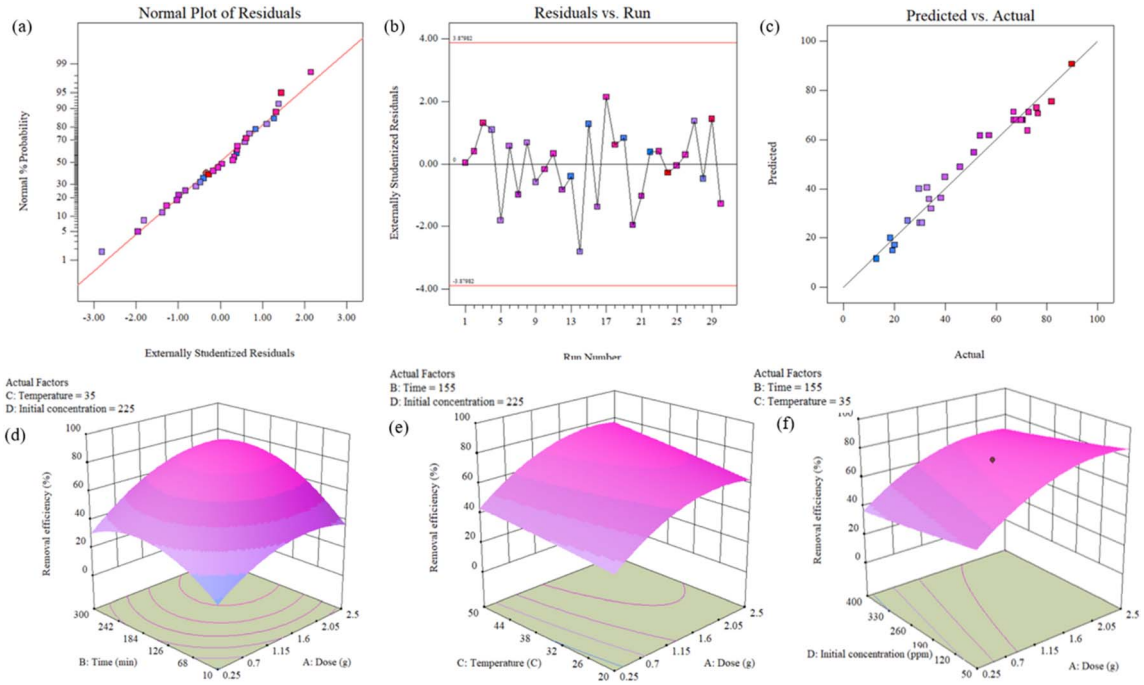

Fig. 5 Residual plots. (a) Normal plot of residuals. (b) Residuals *vs.* runs plot. (c) Predicted *vs.* actual plot. (d) Combined relation of process variables (time and dose). (e) Combined relation of process variables (temperature and dose). (f) Combined relation of process variables (initial concentration and dose) on response (removal efficiency %).

concentration (62 mg l^{-1}), resulting in 89% of Pb^{2+} removal. To affirm optimum parameters, adsorption experimentation was performed under the confidence limit of 95%. The experimental value of removal efficiency for Pb^{2+} adsorption was 84.75%.

3.5. Artificial neural network modelling

The experimental dataset acquired through RSM can effectively be used to assess the ANN model. In addition to evaluate the correlation between input and output parameters, the correlation coefficient and mean square error were also employed to ascertain the predictability of the model.[68] The optimal ANN topology was designed as 4-6-6-1 (an input layer with 4 neurons representing dose, time, temperature, and initial concentration; two hidden layers with 6 neurons each and an output layer corresponding to the removal efficiency). The regression plots of the ANN model for training, validation, testing and all

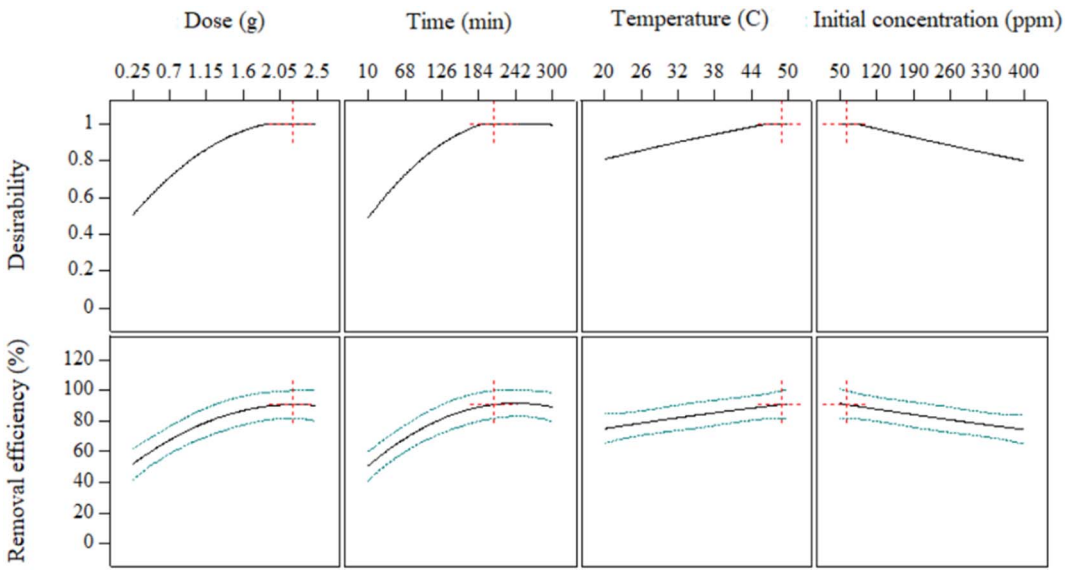

Fig. 6 Plot for the response (removal efficiency %) optimization.

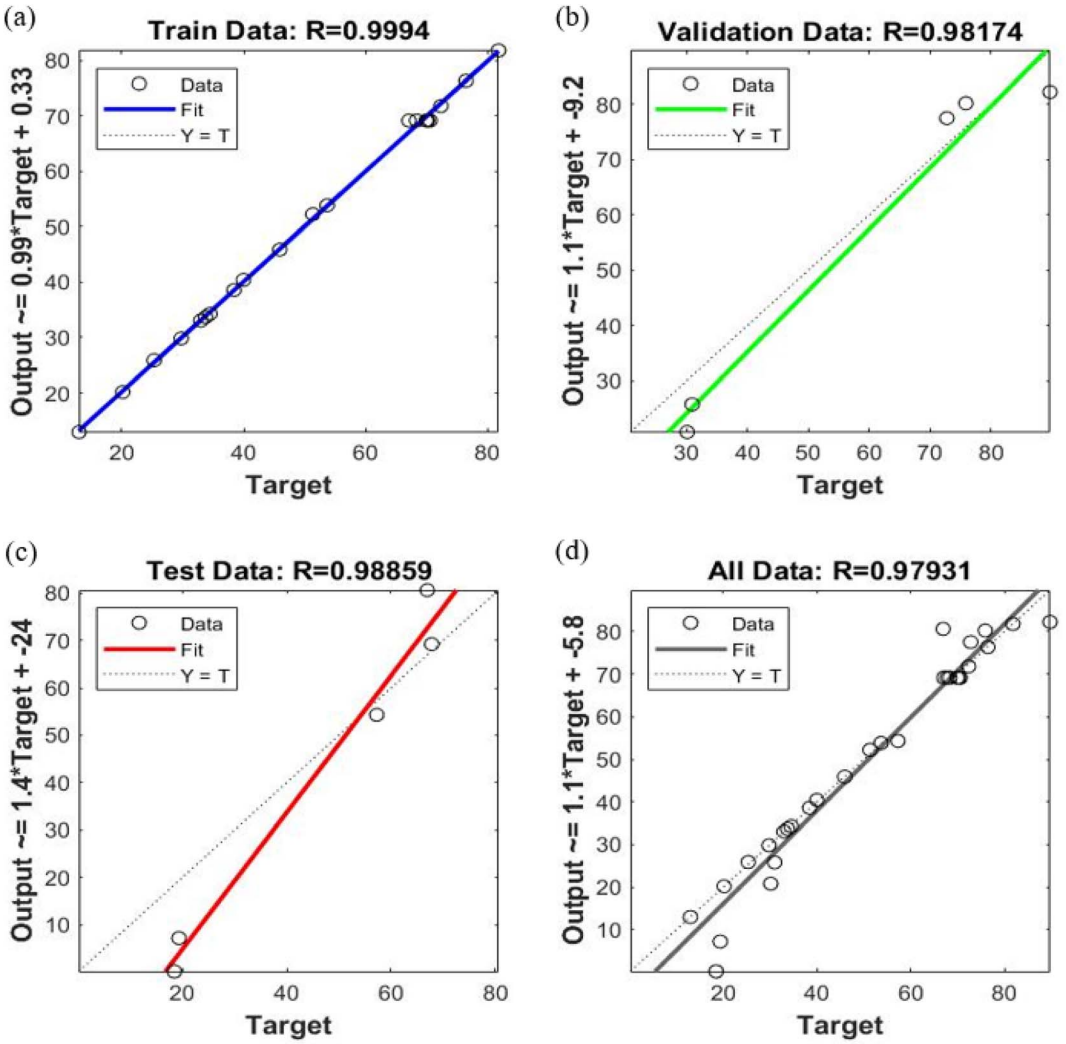

Fig. 7 ANN regression plots for (a) training, (b) validation, (c) testing and (d) all data prediction sets.

prediction data sets are shown in Fig. 7. It is observed that the ANN model established a strong correlation using the training data with an optimized structure with correlation coefficient *i.e.*, 0.9994 as depicted in Fig. 7(a). Additionally, it also performed well using validation and testing data with some scattering. The correlation coefficients for validation and testing are 0.9817 and 0.9885, respectively. It can also be observed that the output values of ANN model lies close to the experimental ones. For an overall prediction, the correlation coefficient is 0.9793; it can be affirmed that the ANN model effectively interpolates the experimental data, indicating its satisfactory performance. The validation performance plot, as shown in Fig. 8, evaluates the training process's reliability. Fig. 8 illustrates the predicted values of normalized removal efficiency through ANN model for both training and testing data compared to the experimental normalized data.

The assessment of the predictive and generalization abilities of both the RSM and ANN models was conducted using their respective R^2 values as mentioned in Table 7. The values of R^2 for both models indicates that they effectively forecast the

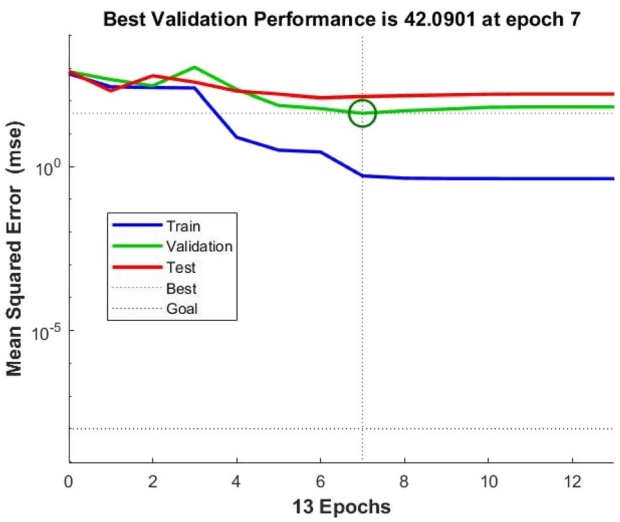

Fig. 8 Performance plot of ANN model (mean square error against number of epochs).

Table 7 Comparison of ANN and RSM

Parameter	ANN	RSM
R^2	0.979	0.960

experimental values as both values approaches unity. Thus, both models are considered as effective in foreseeing the experimental removal efficiency of developed adsorbents.

3.6. Adsorption kinetics

The influence of time on the Pb^{2+} ions adsorption is illustrated in Fig. 9(a), and it was observed that equilibrium is achieved at approximately 120 min. At the initial stage, a steep slope is observed in the curve owing to the high adsorption rate. The initial adsorption rate is considerably high due to many active species on the adsorbent.[69] As the contact time tends to increase, the adsorption rate decreases due to the saturation of the available active species, thus implying that the equilibrium has been accomplished. This situation proves that the adsorption kinetics is based on the rate of adsorbate transferred from the aqueous solution to the surface of the adsorbent.[70,71] Furthermore, the mechanism for the Pb^{2+} ions adsorption on the adsorbent is explored by employing non-linear pseudo first order, pseudo-second order, *n*th order kinetics, Weber and Morris, and Bangham's model to the experimental results. Plots for the respective models are demonstrated in Fig. 9(b)–(d).

The plot shown in Fig. 9(b) depicts the correlation of experimental values with the *n*th-order kinetic model rather than pseudo-first-order and pseudo-second-order kinetics. The model with a minimum error value and higher R^2 is considered the best fit for experimental data.[72] However, the value of SSE implies that the pseudo *n*th-order kinetic model is the best fit for the experimental data of Pb^{2+} adsorption, which predicts the studied adsorption kinetics. The values of R^2 and SSE for *n*th-order kinetics are 0.99 and 0.02, respectively, while SSE for pseudo-first-order and second-order are higher than the *n*th-order kinetics. The value of coefficient "*n*" of *n*th order is approximately 1.14 and is increasing as the initial concentration of Pb^{2+} ions increases in the aqueous solution. This might be due to the concentration gradient *i.e.*, higher Pb^{2+} concentrations at the initial stage.[73,74] The model's fitness reveals that complicated adsorption phenomenon has occurred and there might exist an interaction between the adsorbate and adsorbent.[75,76]

Furthermore, Bangham's model has 0.94 as the value of R^2, which depicts that the model did not conform well with the experimental data, revealing that the pore diffusion phenomena is not dominating the adsorption process.[77] Further, the Pb^{2+} adsorption is likely to be regulated by inter-particle diffusion or

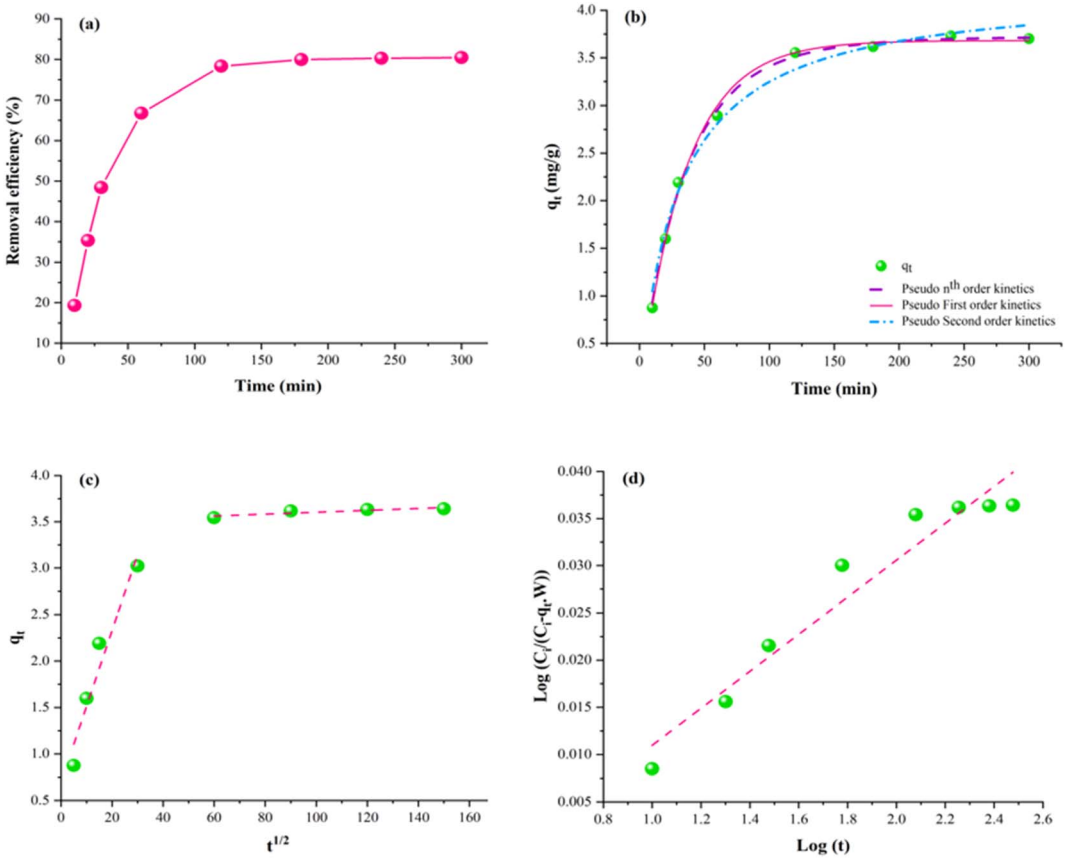

Fig. 9 Kinetic modelling. (a) Effect of time. (b) Non-linear kinetics (pseudo first order, pseudo second order & *n*th-order Kinetics). (c) Intra-particle diffusion model. (d) Bangham's model.

Table 8 Parameters for kinetic models

Kinetic models	Parameters	Values
Pseudo-first-order	q_e (mg g^{-1})	3.62
	k_o (min^{-1})	0.02
	R^2	0.99
Pseudo-second-order	q_e (mg g^{-1})	4.23
	k_1 (g mg^{-1} min^{-1})	0.00
	R^2	0.98
Pseudo-nth order	q_e (mg g^{-1})	3.27
	K_n (min^{-1})	0.02
	N	1.135
	R^2	0.99
Intra particle diffusion	$\varnothing_1$	1.19
	k_{wb} (mg g^{-1} min$^{-1/2}$)	0.44
	R^2	0.84
	$\varnothing_2$	3.6
	$k_{wb'}$ (mg g^{-1} min$^{-1/2}$)	0.0004
	R^2	0.97
Bangham's	k_b (g)	0.99
	δ	1.01
	R^2	0.94

mass transfer. To estimate the rate-determining step, Weber and Morris (WM) model is applied.[78] The WM model divides the adsorption process into two steps. The steep curve represents the immediate reaction step dominated by the surface diffusion phenomena in the first step. The second step exhibits a slow reaction step governed by the pore diffusion phenomena.[79] It is evident from Table 8 that the value of $\varnothing_1$ is less than the $\varnothing_2$, and k_{wb} has a higher value than $k_{wb'}$. This suggests that the reaction is slowest in the second step owing to the greater thickness of the boundary layer, which leads to a larger $\varnothing_2$. Thus, it is concluded that the interparticle diffusion phenomenon is the rate-determining step in Pb^{2+} adsorption.[31,80]

Intercept and slope of the above-illustrated plots are utilized for estimating the pertinent parameters of each model, and their respective correlation coefficient is summarized in Table 8.

3.7. Adsorption thermodynamics

The influence of temperature on Pb^{2+} adsorption is presented in Fig. 10(a), which depicts that elevation in temperature directly

Table 9 Thermodynamics parameters for the Pb^{2+} adsorption

$\Delta G'$ (kJ mol^{-1})				$\Delta S'$	$\Delta H'$
293 K	303 K	313 K	323 K	(J mol^{-1} K^{-1})	(kJ mol^{-1})
−0.51	−1.71	−2.67	−4.63	0.124	38.37

impacts the Pb^{2+} adsorption. This indicates that an increase in temperature results in an increase in Pb^{2+} adsorption.[81] The rate of diffusion of adsorbate molecules is significantly enhanced within the pores and across the adsorbent's boundary layer owing to the temperature increase. This reduces the resistance against mass transfer, allowing the increased adsorbate molecule's mobility within the pores and across the boundary layer.[82,83]

The thermodynamic behavior of the developed adsorbent is shown in Fig. 10(b) as Van't Hoff plot, and the calculated parameters are compiled in Table 9. The positive value of $\Delta S'$ reveals the upsurge in augmented randomness around the adsorbent–adsorbate interface initiated by the adsorption. Furthermore, the $\Delta S'$ has a low value, indicating that this system does not bring about any substantial change in entropy.[84] The positive enthalpy value indicates the endothermic nature of the Pb^{2+} adsorption process.[85] The negative $\Delta G'$ values exhibit the spontaneity of the Pb^{2+} adsorption process. The $\Delta G'$ values tend to decrease with an elevation in temperature, indicating that adsorption's spontaneity lowers at lower temperatures. The thermodynamic study suggests that the increasing temperature implies in an increased adsorption.[85]

The negative $\Delta G'$ values exhibit the spontaneity of the adsorption process. The $\Delta G'$ values tend to decrease with an elevation in temperature, indicating that adsorption's spontaneity lowers at lower temperatures. The thermodynamic study suggests that the Pb^{2+} adsorption process is feasible, and the increase in temperature implies an increase in adsorption.[86,87]

3.8. Adsorption isotherms

The non-linear Langmuir and Freundlich isotherm models are employed on experimental data for the adsorption of Pb^{2+}. The

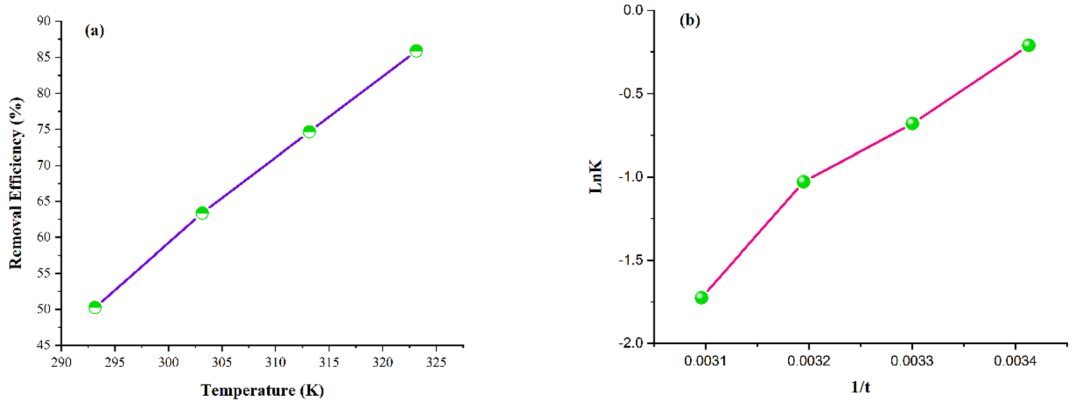

Fig. 10 Adsorption thermodynamics plots. (a) Effect of temperature on the Pb^{2+} adsorption. (b) Van't Hoff plot.

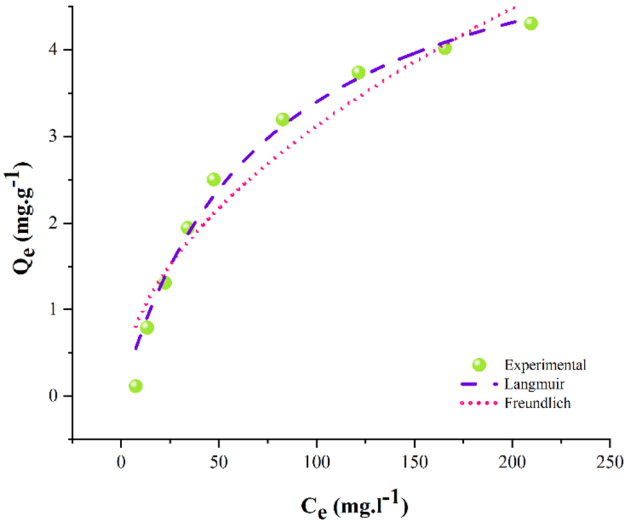

Fig. 11 Non-linear Langmuir, and Freundlich isotherms.

Table 10 Parameters calculated using isotherm models

	Parameters				
Isotherm models	q_{max} (mg g^{-1})	K_l	K_F (l g^{-1})	α	R^2
Langmuir	5.90	0.014	—	—	0.98
Freundlich	—	—	0.28	1.91	0.93

pertinent correlation coefficients (R^2) and parameters were estimated using Origin Pro (version 2021) software. The plots of isotherms are represented in Fig. 11, while the respective parameters for these isotherms are compiled in Table 10. The fitness of isotherm models is based on the value of R^2.[88] The parameters portray that the Langmuir isotherm fits well with the experimental data, having significantly higher R^2 than the Freundlich isotherm. This depicts that the adsorbent's surface is homogenous with a Langmuir monolayer capacity of 5.90 mg g^{-1}.[89]

The R^2 of Freundlich is lower than that of Langmuir's *i.e.*, 0.98. Hence, Table 10 reveals the order of model fitness as Langmuir > Freundlich. The Freundlich model was ruled out owing to poor fitness on the data. The separation factor for Langmuir (K_l) is 0.014 which is dimensionless that is higher than zero and less than 1, which suggests the Pb^{2+} adsorption is favorable on the adsorbent.[90–92] If K_l is greater than 1, the adsorption is considered unfavorable, while if $K_l = 0$, it means the adsorption is irreversible.[93] It is concluded that the Pb^{2+} adsorption is homogenous and monolayer as the Langmuir model postulates that monolayer adsorption occurs at homogenous adsorption sites of the adsorbent.[94]

The adsorption mechanism is a complex and multistep process as experimental values follows the *n*th-order kinetic model and Langmuir isotherm. The *n*th-order kinetic model indicates a high dependence on Pb^{2+} ions concentration. While combining both models, the adsorption process likely initiates with swift adsorption (as indicated by the *n*th-order kinetics),

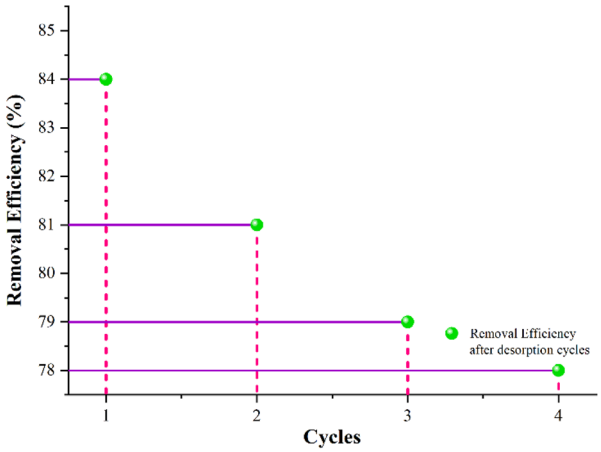

Fig. 12 Removal efficiencies of developed adsorbent after adsorption–desorption cycles.

where adsorbate molecules promptly occupy surface sites. As saturation approaches, adsorption gradually slows down, transitioning into a regulated formation of a monolayer on the adsorbent's surface, which is consistent with the findings of the Langmuir model.

3.9. Regeneration study of adsorbent

Regeneration study aids in elucidating the nature of adsorption and allows for the regeneration of the adsorbed heavy metal ions from the adsorbent; thus, the adsorbent can be further used repeatedly.[95] In order to regenerate the developed adsorbent, Pb^{2+} ions adsorbed on the adsorbent can be efficiently removed in a beaker. The beaker contains 100 ml of 5% NaOH aqueous solution and is placed in a mechanical shaker at a speed of 80 rpm at 60 °C for 60 minutes.[96] The regenerated adsorbent was then used in the adsorption–desorption. Adsorption–desorption cycles of the developed adsorbent were repeated up to 4 times and evaluated the adsorption capacity after each cycle. The developed adsorbent was regenerated in its original form, and its performance is mentioned in Fig. 12 below.

4 Conclusion

Zeolite and activated MWCNTs were successfully embedded in PAN nanofibers *via* needleless electrospinning. The as-prepared nanofibrous adsorbent improved adsorption efficiency for Pb^{2+} ions. The prepared adsorbents were characterized to confirm the incorporation of zeolite and activated MWCNTs into the PAN nanofibrous matrix. By increasing the concentration of additives, the surface of nanofibers becomes rougher than at lower concentrations, as evidenced by SEM micrographs. FTIR analysis confirmed the successful incorporation of zeolite and activated MWCNTs. The thermodynamic and isotherm studies revealed that the Pb^{2+} adsorption is endothermic and followed Langmuir isotherm with q_{max}, *i.e.*, 5.90 mg g^{-1}. The kinetic study showed that the adsorption process was dominated by pseudo first-order kinetics and accompanied by interparticle

diffusion as the rate-limiting step. The prepared adsorbent has good regeneration ability and has 78% removal efficiency after 4 cycles. Thus, the proposed adsorbent can potentially adsorb Pb^{2+} ions from water.

Informed consent

All subjects participating in the research gave their informed consent.

Data availability

Information is available upon request.

Author contributions

Conceptualization, U. M. and A. N.; methodology, U. M.; software, M. J.; validation, T. H.; formal analysis, S. F. and M. J.; investigation, U. M., A. N.; resources, T. H. and A. S. A.; data curation, Z. K.; writing original draft, U. M.; review and editing, A. N., M. B. Q., and T. H.; visualization, Z. K. and S. F.; supervision, M. B. Q., A. N., and T. H.; project administration, M. B. Q. and A. N. All authors have read and agreed to the published version of the manuscript.

Conflicts of interest

There are no conflicts to declare.

Acknowledgements

The authors are thankful to the Deanship of Scientific Research under supervision of the Science and Engineering Research Center at Najran University for funding this work under the research centers funding program with grant (NU/RCP/SERC/12/9) and Pakistan Science Foundation (PSF) under the grant number (PSF/CRP/P-NTU-HELIX-194).

References

1 M. Vakili, S. Deng, G. Cagnetta, W. Wang, P. Meng, D. Liu and G. Yu, *Sep. Purif. Technol.*, 2019, **224**, 373–387.
2 K. K. Kesari, R. Soni, Q. M. S. Jamal, P. Tripathi, J. A. Lal, N. K. Jha, M. H. Siddiqui, P. Kumar, V. Tripathi and J. Ruokolainen, *Water, Air, Soil Pollut.*, 2021, **232**, 1–28.
3 S. S. Fiyadh, M. A. AlSaadi, W. Z. Jaafar, M. K. AlOmar, S. S. Fayaed, N. S. Mohd, L. S. Hin and A. El-Shafie, *J. Cleaner Prod.*, 2019, **230**, 783–793.
4 S. Rajeshkumar, Y. Liu, X. Zhang, B. Ravikumar, G. Bai and X. Li, *Chemosphere*, 2018, **191**, 626–638.
5 H. Zandavar, S. M. Pourmortazavi and S. Mirsadeghi, *J. Mater. Res. Technol.*, 2021, **13**, 25–37.
6 Z. Rahman and V. P. Singh, *Environ. Monit. Assess.*, 2019, **191**, 1–21.
7 K. L. Hon, C. K. Fung and K. C. Leung Alexander, *Hong Kong Med. J.*, 2017, **23**, 616–621.
8 A. A. Alshahrani, M. AlQahtani, A. M. Almushaikeh, H. M. A. Hassan, M. Alzaid, A. N. Alrashidi and I. H. Alsohaimi, *J. Mater. Res. Technol.*, 2022, **18**, 2310–2319.
9 A. Wołowicz, K. Staszak and Z. Hubicki, *J. Water Process Eng.*, 2023, **53**, 103792.
10 Z. Yang, Y. Sun, Z. Hou, H. Yu, M. Li, Y. Li, Y. Li, B. Gao and S. Xu, *J. Hazard. Mater.*, 2023, **447**, 130768.
11 X. Long, G.-Q. Zhao, Y. Zheng, J. Hu, Y. Zuo, W. Luo and F. Jiao, *Chem. Eng. J.*, 2023, 144904.
12 Z. Raji, A. Karim, A. Karam and S. Khalloufi, *Trends Food Sci. Technol.*, 2023, **137**, 74–91.
13 S. R. Al-Mhyawi, D. M. D. Bader, M. A. Bajaber, S. M. A. El Dayem, A. H. Ragab, K. A. Abd El-Rahem, M. A. Gado, B. M. Atia and M. F. Cheira, *J. Mater. Res. Technol.*, 2023, **22**, 3058–3074.
14 L. Velarde, M. S. Nabavi, E. Escalera, M. L. Antti and F. Akhtar, *Chemosphere*, 2023, **328**, 138508.
15 K. Ahmad, H. u. R. Shah, M. S. Khan, A. Iqbal, E. Potrich, L. S. Amaral, S. Rasheed, H. Nawaz, A. Ayub, K. Naseem, A. Muhammad, M. R. Yaqoob and M. Ashfaq, *J. Cleaner Prod.*, 2022, **368**, 133010.
16 U. O. Aigbe, K. E. Ukhurebor, R. B. Onyancha, O. A. Osibote, H. Darmokoesoemo and H. S. Kusuma, *J. Mater. Res. Technol.*, 2021, **14**, 2751–2774.
17 K. Tomasz, K. Anna and C. Ryszard, *Microchem. J.*, 2019, **145**, 1011–1025.
18 N. Abdullah, N. Yusof, A. F. Ismail, F. E. C. Othman, J. Jaafar, L. W. Jye, W. N. W. Salleh, F. Aziz and N. Misdan, *Emergent Mater.*, 2018, **1**, 89–94.
19 N. R. Mikal, S. Sadjadi, M. Rajabi-Hamane, S. J. Ahmadi and E. Iravani, *J. Iran. Chem. Soc.*, 2016, **13**, 763–771.
20 Z. Aslam, I. A. Hussein, R. A. Shawabkeh, M. A. Parvez, W. Ahmad and Ihsanullah, *J. Air Waste Manage. Assoc.*, 2019, **69**, 246–257.
21 J. A. A. Abdullah, V. Perez-Puyana, A. Guerrero and A. Romero, *J. Appl. Polym. Sci.*, 2023, **140**, e54345.
22 A. Malekian and N. Chitsaz, *Advances in Streamflow Forecasting*, 2021, pp. 115–147.
23 S. S. Fiyadh, S. M. Alardhi, M. Al Omar, M. M. Aljumaily, M. A. Al Saadi, S. S. Fayaed, S. N. Ahmed, A. D. Salman, A. H. Abdalsalm, N. M. Jabbar and A. El-Shafi, *Heliyon*, 2023, **9**, e15455.
24 C. E. Onu, J. T. Nwabanne, P. E. Ohale and C. O. Asadu, *S. Afr. J. Chem. Eng.*, 2021, **36**, 24–42.
25 I. Mironyuk, I. Mykytyn, H. Vasylyeva and K. Savka, *J. Mol. Liq.*, 2020, **316**, 113840.
26 L. Qiao, S. Li, Y. Li, Y. Liu and K. Du, *J. Cleaner Prod.*, 2020, **253**, 120017.
27 U. A. Edet and A. O. Ifelebuegu, *Process*, 2020, **8**, 1–15.
28 N. Sadeu Christian, S. Gabche Anagho, C. Sadeu Ngakou, G. Solomon Anagho, H. Manga Ngomo, M. Raziq Rahimi Kooh and U. Brunei Darussalam, *Curr. J. Appl. Sci. Technol.*, 2019, **36**, 1–18.
29 A. Hashem, S. M. Badawy, S. Farag, L. A. Mohamed, A. J. Fletcher and G. M. Taha, *J. Environ. Chem. Eng.*, 2020, **8**, 103966.

30 A. Nasrullah, A. H. Bhat, A. Naeem, M. H. Isa and M. Danish, *Int. J. Biol. Macromol.*, 2018, **107**, 1792–1799.
31 A. L. P. F. Caroni, C. R. M. de Lima, M. R. Pereira and J. L. C. Fonseca, *J. Colloid Interface Sci.*, 2009, **340**, 182–191.
32 S. Jiang, T. Yu, R. Xia, X. Wang and M. Gao, *Mater. Chem. Phys.*, 2019, **232**, 374–381.
33 B. Li, Q. Zhang and C. Ma, *Int. J. Chem. Eng.*, 2021, **2021**, 8886646.
34 B. C. Kelly, *Astrophys. J.*, 2007, **665**, 519947.
35 N. R. V. Derick, D. E. P. Sumalapao, J. R. Distor, I. D. Ditan, N. T. S. Domingo and L. F. Dy, *J. Math. Comput. Sci.*, 2016, **6**, 1157–1168.
36 A. Zahir, Z. Aslam, M. S. Kamal, W. Ahmad, A. Abbas and R. A. Shawabkeh, *J. Mol. Liq.*, 2017, **244**, 211–218.
37 S. Zarin, Z. Aslam, A. Zahir, M. S. Kamal, A. G. Rana, W. Ahmad and S. Ahmed, *J. Iran. Chem. Soc.*, 2018, **15**, 2689–2701.
38 Y. P. Zhang, V. S. K. Adi, H. L. Huang, H. P. Lin and Z. H. Huang, *J. Ind. Eng. Chem.*, 2019, **76**, 240–244.
39 M. Malhotra, S. Suresh and A. Garg, *Environ. Sci. Pollut. Res.*, 2018, **25**, 32210–32220.
40 M. N. Sahmoune, *Environ. Chem. Lett.*, 2019, **17**, 697–704.
41 N. Hoogesteijn von Reitzenstein, B. Sonmez Baghirzade, E. Pruitt, K. Hristovski, P. Westerhoff and O. G. Apul, *Chem. Eng. J. Adv.*, 2022, **9**, 100199.
42 S. Swaminathan, N. M. Imayathamizhan and A. Muthumanickkam, *J. Elastomers Plast.*, 2020, **53**, 48–67.
43 S. Subramani and S. Rajiv, *Ionics*, 2021, **27**, 2203–2218.
44 S. Subramani and S. Rajiv, *Ionics*, 2021, **27**, 2203–2218.
45 A. Bayat, A. Tati, S. Ahmadipouya, S. A. Haddadi and M. Arjmand, *J. Mol. Liq.*, 2021, **331**, 115734.
46 M. Goswami and P. Phukan, *J. Environ. Chem. Eng.*, 2017, **5**, 3508–3517.
47 M. Koosha and H. Mirzadeh, *J. Biomed. Mater. Res., Part A*, 2015, **103**, 3081–3093.
48 S. Kalantari, F. Golbabaei, M. Reza Monazzam, A. Ghasemi Koozekonan, M. Reza Monazzam Esmaeilpour, S. Kalantary, A. Karimi, K. Azam and V. Ahmadi Moshiran, *J. Text. Inst.*, 2021, **112**, 946–954.
49 S. M. Abegunde, K. S. Idowu, O. M. Adejuwon and T. Adeyemi-Adejolu, *Resour. Environ. Sustain.*, 2020, **1**, 100001.
50 K. Zhang, Z. Dai, W. Zhang, Q. Gao, Y. Dai, F. Xia and X. Zhang, *Coord. Chem. Rev.*, 2021, **434**, 213809.
51 B. Huang, G. Liu, P. Wang, X. Zhao and H. Xu, *Processes*, 2019, **7**, 167.
52 R. A. S. Rizwan Ali, Z. Aslam and I. A. H. Anam Asghar, *Turk. J. Chem.*, 2020, **44**, 279–295.
53 L. Cui, Y. Wang, L. Gao, L. Hu, L. Yan, Q. Wei and B. Du, *Chem. Eng. J.*, 2015, **281**, 1–10.
54 M. Kragović, M. Stojmenović, J. Petrović, J. Loredo, S. Pašalić, A. Nedeljković and I. Ristović, *Procedia Manuf.*, 2019, **32**, 286–293.
55 S. Zarin, Z. Aslam, A. Zahir, M. S. Kamal, A. G. Rana, W. Ahmad and S. Ahmed, *J. Iran. Chem. Soc.*, 2018, **15**, 2689–2701.
56 A. Aichour and H. Zaghouane-Boudiaf, *Microchem. J.*, 2019, **146**, 1255–1262.
57 C. Aniagor, A. Hashem, C. Onyeka Aniagor, M. Fathi Nasr and A. Abou-Okeil, *Int. J. Biol. Macromol.*, 2018, 1–16.
58 D. Kouotou, M. Ghalit, J. N. Ndi, L. M. P. Martinez, M. El Ouahabi, J. M. Ketcha and E. K. Gharibi, *Environ. Monit. Assess.*, 2021, **193**, 1–15.
59 M. Mourabet, A. El Rhilassi, H. El Boujaady, M. Bennani-Ziatni and A. Taitai, *Arabian J. Chem.*, 2017, **10**, S3292–S3302.
60 N. Sohrabi, R. Mohammadi, H. R. Ghassemzadeh and S. S. S. Heris, *J. Mol. Liq.*, 2021, **328**, 115384.
61 D. Allouss, Y. Essamlali, O. Amadine, A. Chakir and M. Zahouily, *RSC Adv.*, 2019, **9**, 37858–37869.
62 Z. Wang, Y. Jia, W. Song, X. Li, K. Xu and Z. Wang, *J. Cleaner Prod.*, 2021, **300**, 126974.
63 A. A. H. Saeed, N. Y. Harun, S. Sufian, M. R. Bilad, B. A. Nufida, N. M. Ismail, Z. Y. Zakaria, A. H. Jagaba, A. A. S. Ghaleb and B. N. S. Al-Dhawi, *Water*, 2021, **13**, 999.
64 S. Z. N. Ahmad, W. N. Wan Salleh, A. F. Ismail, N. Yusof, M. Z. Mohd Yusop and F. Aziz, *Chemosphere*, 2020, **248**, 126008.
65 N. K. Soliman and A. F. Moustafa, *J. Mater. Res. Technol.*, 2020, **9**, 10235–10253.
66 R. V. Hemavathy, A. Saravanan, P. S. Kumar, D. V. N. Vo, S. Karishma and S. Jeevanantham, *Chemosphere*, 2021, **283**, 131276.
67 Z. Wang, Y. Jia, W. Song, X. Li, K. Xu and Z. Wang, *J. Cleaner Prod.*, 2021, **300**, 126974.
68 A. Nighojkar, K. Zimmermann, M. Ateia, B. Barbeau, M. Mohseni, S. Krishnamurthy, F. Dixit and B. Kandasubramanian, *Environ. Sci.: Adv.*, 2023, **2**, 11–38.
69 P. B. Vilela, A. Dalalibera, E. C. Duminelli, V. A. Becegato and A. T. Paulino, *Environ. Sci. Pollut. Res.*, 2019, **26**, 28481–28489.
70 R. S. Bangari, A. Yadav and N. Sinha, *Soft Matter*, 2021, **17**, 2640–2651.
71 A. Dargahi, M. R. Samarghandi, A. Shabanloo, M. M. Mahmoudi and H. Z. Nasab, *Biomass Convers. Biorefin.*, 2021, 1–15.
72 A. Zahir, Z. Aslam, U. Aslam, A. Abdullah, R. Ali and M. M. Bello, *Chem. Biochem. Eng. Q.*, 2020, **34**, 93–104.
73 S. Haykin, *IEEE J. Sel. Area. Commun.*, 2005, **23**, 201–220.
74 R. L. Tseng, P. H. Wu, F. C. Wu and R. S. Juang, *Chem. Eng. J.*, 2014, **237**, 153–161.
75 Y. Tanimoto and S. I. Noro, *RSC Adv.*, 2021, **11**, 23707–23713.
76 Z. Yang, G. Wu, Q. Li, H. Ai, X. Yao and H. Ji, *Sep. Sci. Technol.*, 2021, **56**, 860–869.
77 M. Benjelloun, Y. Miyah, G. Akdemir Evrendilek, F. Zerrouq and S. Lairini, *Arabian J. Chem.*, 2021, **14**, 103031.
78 T. R. Sahoo and B. Prelot, in *Nanomaterials for the Detection and Removal of Wastewater Pollutants*, Elsevier, 2020, pp. 161–222.
79 X. Liu, Y. Zhang, Y. Liu and T. Zhang, *Polym. Bull.*, 2022, 1–20.
80 J. López-Luna, L. E. Ramírez-Montes, S. Martinez-Vargas, A. I. Martínez, O. F. Mijangos-Ricardez, M. d. C. A. González-Chávez, R. Carrillo-González,

F. A. Solís-Domínguez, M. d. C. Cuevas-Díaz and V. Vázquez-Hipólito, *SN Appl. Sci.*, 2019, **1**, 1–19.
81 K. Kayalvizhi, N. M. I. Alhaji, D. Saravanakkumar, S. B. Mohamed, K. Kaviyarasu, A. Ayeshamariam, A. M. Al-Mohaimeed, M. R. AbdelGawwad and M. S. Elshikh, *Environ. Res.*, 2022, **203**, 111814.
82 T. C. Egbosiuba, A. S. Abdulkareem, J. O. Tijani, J. I. Ani, V. Krikstolaityte, M. Srinivasan, A. Veksha and G. Lisak, *Chemosphere*, 2021, **266**, 128937.
83 S. Pandey, E. Fosso-Kankeu, M. J. Spiro, F. Waanders, N. Kumar, S. S. Ray, J. Kim and M. Kang, *Mater. Today Chem.*, 2020, **18**, 100376.
84 S. Khan, M. Idrees and M. Bilal, *Colloids Surf., A*, 2021, **623**, 126711.
85 G. Hanbali, S. Jodeh, O. Hamed, R. Bol, B. Khalaf, A. Qdemat, S. Samhan and O. Dagdag, *Processes*, 2020, **8**, 986.
86 M. Zulfiqar, S. Y. Lee, A. A. Mafize, N. A. M. A. Kahar, K. Johari and N. E. Rabat, *Polymers*, 2020, **12**, 430.
87 S. F. Abo-Zahra, I. M. Abdelmonem, T. E. Siyam, A. M. El-Masry and H. M. Abdel-Aziz, *Polym. Bull.*, 2022, **79**, 4395–4415.
88 B. O. Isiuku, P. C. Okonkwo and C. D. Emeagwara, *J. Dispers. Sci. Technol.*, 2021, **42**, 1879–1897.
89 A. Zahir, Z. Aslam, M. S. Kamal, W. Ahmad, A. Abbas and R. A. Shawabkeh, *J. Mol. Liq.*, 2017, **244**, 211–218.
90 K. Kayalvizhi, N. M. I. Alhaji, D. Saravanakkumar, S. B. Mohamed, K. Kaviyarasu, A. Ayeshamariam, A. M. Al-Mohaimeed, M. R. AbdelGawwad and M. S. Elshikh, *Environ. Res.*, 2022, **203**, 111814.
91 A. Kokalj, *Corros. Sci.*, 2023, **217**, 111124.
92 Ş. Altun, A. E. Kadak, A. Küçükgülmez, O. Gülnaz and M. Çelik, *Toxicol. Res.*, 2023, **39**, 127–133.
93 N. Hasani, T. Selimi, A. Mele, V. Thaçi, J. Halili, A. Berisha and M. Sadiku, *Molecules*, 2022, **27**, 1856.
94 A. Hashem, C. O. Aniagor, G. M. Taha and M. Fikry, *Curr. Res. Green Sustainable Chem.*, 2021, **4**, 100056.
95 O. Pereao, C. Bode-Aluko, K. Laatikainen, A. Nechaev and L. Petrik, *J. Polym. Environ.*, 2019, **27**, 1843–1860.
96 Y. Luo, M. Liu, Y. Chen, T. Wang and W. Zhang, *R. Soc. Open Sci.*, 2019, **6**, 190764.